Focus Section: Data Mine: 2019 Ridgecrest, California Earthquake Sequence

Airborne Lidar and Electro-Optical Imagery along Surface Ruptures of the 2019 Ridgecrest Earthquake Sequence, Southern California

Kenneth W. Hudnut[*1], Benjamin A. Brooks[2], Katherine Scharer[1], Janis L. Hernandez[3], Timothy E. Dawson[4], Michael E. Oskin[5], J. Ramon Arrowsmith[6], Christine A. Goulet[7], Kelly Blake[8], Matthew L. Boggs[9], Stephan Bork[10], Craig L. Glennie[11], Juan Carlos Fernandez-Diaz[11], Abhinav Singhania[11], Darren Hauser[11], and Sven Sorhus[11]

Abstract

Surface rupture from the 2019 Ridgecrest earthquake sequence, initially associated with the M_w 6.4 foreshock, occurred on 4 July on a ~17 km long, northeast–southwest-oriented, left-lateral zone of faulting. Following the M_w 7.1 mainshock on 5 July (local time), extensive northwest–southeast-oriented, right-lateral faulting was then also mapped along a ~50 km long zone of faults, including subparallel splays in several areas. The largest slip was observed in the epicentral area and crossing the dry lakebed of China Lake to the southeast. Surface fault rupture mapping by a large team, reported elsewhere, was used to guide the airborne data acquisition reported here. Rapid rupture mapping allowed for accurate and efficient flight line planning for the high-resolution light detection and ranging (lidar) and aerial photography. Flight line planning trade-offs were considered to allocate the medium (25 pulses per square meter [ppsm]) and high-resolution (80 ppsm) lidar data collection polygons. The National Center for Airborne Laser Mapping acquired the airborne imagery with a Titan multispectral lidar system and Digital Modular Aerial Camera (DiMAC) aerial digital camera, and U.S. Geological Survey acquired Global Positioning System ground control data. This effort required extensive coordination with the Navy as much of the airborne data acquisition occurred within their restricted airspace at the China Lake ranges.

Cite this article as Hudnut, K. W., B. A. Brooks, K. Scharer, J. L. Hernandez, T. E. Dawson, M. E. Oskin, J. Ramon Arrowsmith, C. A. Goulet, K. Blake, M. L. Boggs, *et al.* (2020). Airborne Lidar and Electro-Optical Imagery along Surface Ruptures of the 2019 Ridgecrest Earthquake Sequence, Southern California, *Seismol. Res. Lett.* **XX**, 1–12, doi: 10.1785/0220190338.

Introduction

Aerial spatial and spectral data sets, including highly accurate topographic light detection and ranging (lidar) data and high-resolution digital photographs, were acquired along the full extents of surface fault ruptures associated with the 2019 Ridgecrest earthquake sequence. The complex pattern of surface fault ruptures associated with the M_w 6.4 foreshock and M_w 7.1 mainshock, forming an overall lambda-shaped map pattern, was covered comprehensively at variable resolutions that are described in detail in this article. Accurate georeferencing of the lidar and orthoimagery products, through use of a ground-based network of geodetic control stations and airborne Global Navigation Satellite Systems (GNSS) and inertial sensors, was performed to a specification of within 12–18 cm horizontally and 5–15 cm vertically. Such high-quality imagery also helps to understand, and document with high fidelity, how the faults broke to the ground surface during the time frame of the earthquake sequence. Geodetic quality ground control results in accurately georeferenced base imagery (also known

1. U.S. Geological Survey, Pasadena, California, U.S.A.; 2. U.S. Geological Survey, Moffett Field, California, U.S.A.; 3. California Geological Survey, Los Angeles, California, U.S.A.; 4. California Geological Survey, San Mateo, California, U.S.A.; 5. Earth and Planetary Sciences Department, University of California, Davis, Davis, California, U.S.A.; 6. School of Earth and Space Exploration, Arizona State University, Tempe, Arizona, U.S.A.; 7. Southern California Earthquake Center, University of Southern California, Los Angeles, California, U.S.A.; 8. Geothermal Program Office, NAVFAC EXWC, NAWS China Lake, China Lake, California, U.S.A.; 9. Naval Air Warfare Center - Weapons Division, China Lake, California, U.S.A.; 10. Water Quality Program, NAVFAC-SW, NAWS China Lake, Environmental Management Division, China Lake, California, U.S.A.; 11. University of Houston, NCALM, Houston, Texas, U.S.A.

*Corresponding author: hudnut@usgs.gov

as geodata) that, in turn, helps to more accurately and fully document the fault surface rupture.

Reconnaissance of rupture pattern guides imagery acquisition

As soon as an earthquake occurs, it is of paramount importance to obtain a synoptic overview of the surface fault rupture, for several purposes. One such purpose is to guide high-resolution geodata acquisition, as was done in the current study of the Ridgecrest earthquake. That is, within less than 30 hr after the M_w 6.4 earthquake, both ground-based and helicopter-based reconnaissance had been accomplished, and high-resolution aerial geotagged photographs had been acquired. Then, after the M_w 7.1 mainshock occurred, two teams deployed toward the northwest and southeast (on two helicopters) so that within one full day the mainshock rupture extent had been surveyed and initially photographed. Although these rapidly obtained aerial and ground-based photos are useful for preserving details of features such as the sharp edges of the surficial cracks very soon after they were formed, such photographs are typically relatively limited in the consistency of their scale and georeferencing and benefit from being augmented with geodetically controlled airborne and space-based remote sensing. Typically, the geotags associated with photos taken during the reconnaissance stage are from handheld Global Position System [GPS] and Global Navigation Satellite System [GNSS] receivers that are either L1 C/A—only or perhaps wide area augmentation system enabled receivers. The positions of the photos are known to within several meters at the best (and typically the orientation and pointing angles of the camera are not recorded).

Data covering the Ridgecrest fault surface ruptures

In this article, we present and describe our approach for the collection and geodetic control of fixed-wing lidar at multiple resolutions and aerial mapping grade photography, that is, nadir pointing and stereo-overlapped. Both data sets span and include the surface fault ruptures associated with the bulk of the Ridgecrest earthquake sequence. We obtained these geodata beginning three weeks after the 5 July (local time) mainshock (27 July–2 August 2019).

Scientific motivation

Mapping of earthquake surface ruptures provides essential information for understanding fault mechanics and hazard. The Ridgecrest earthquake sequence has presented a rare opportunity to apply modern airborne imaging methods to help quantify surface ruptures and near-field effects with unprecedented detail. In combination with the large ground-based team effort to map the surface ruptures and to document them using structure from motion (SfM) stereo photogrammetry, the airborne lidar data and orthoimagery described here provides the accurately geodetically referenced and quantitative geodata framework upon which the wealth of field observations will be mapped for final products.

The nature of these lidar and orthoimagery data sets, and their open availability, can lead to innovative applications for measuring fault slip and its variation along the surface fault ruptures, for example, Hudnut *et al.* (2002), Borsa and Minster (2012), Nissen *et al.* (2012), Oskin *et al.* (2012), Quigley *et al.* (2012), Duffy *et al.* (2013), Glennie *et al.* (2014), and Scott *et al.* (2018, 2019). Such observations may be used to better inform our understanding of the physics of the earthquake source as well as displacement hazard from ground rupture (e.g., Baize *et al.*, 2019).

Scientific issues to be addressed using the airborne geodata include the following:

1. defining rupture geometry and width, with implications for understanding shallow slip deficits and surface fault rupture hazard,
2. measuring distributed cracking indicated by Interferometric Synthetic Aperture Radar to assess fracture mode and stress conditions of this widely distributed anelastic deformation,
3. measuring directly the fault-slip vector from displaced microtopographic features, enhanced with high-resolution surveys of the main fault traces,
4. detecting warping, using differential lidar, of the ground surface in response to slip heterogeneity and distributed yielding, and
5. quantifying liquefaction-induced ground failure and toppling of fragile geologic features by ground motions.

Overview of the Ridgecrest Earthquake Sequence Geodata Acquisition

Geodata were acquired covering the fault surface rupture areas shown in Figure 1 showing the areas-of-interest (AOI) polygons. The orange AOI polygon, that is the larger one, specifies the area over which lidar data were acquired at a specification of 25 pulses per square meter (ppsm). Along the primary surficial fault ruptures, tighter polygons shown in light yellow and light green were covered by lidar at 80 ppsm. The lidar data are provided in the form of a classified lidar point cloud, from which digital surface model (DSM) and digital terrain models are produced. Such geodata products are further described in this article and in metadata on the websites (see Data and Resources).

Airborne laser scanning technology has evolved over the last 20 yr of its application for fault mapping. Early lidar data sets such as the B4 (Bevis *et al.*, 2005) lidar data acquired in 2005 along the southern San Andreas and San Jacinto fault zones in southern California; see Data and Resources, typically

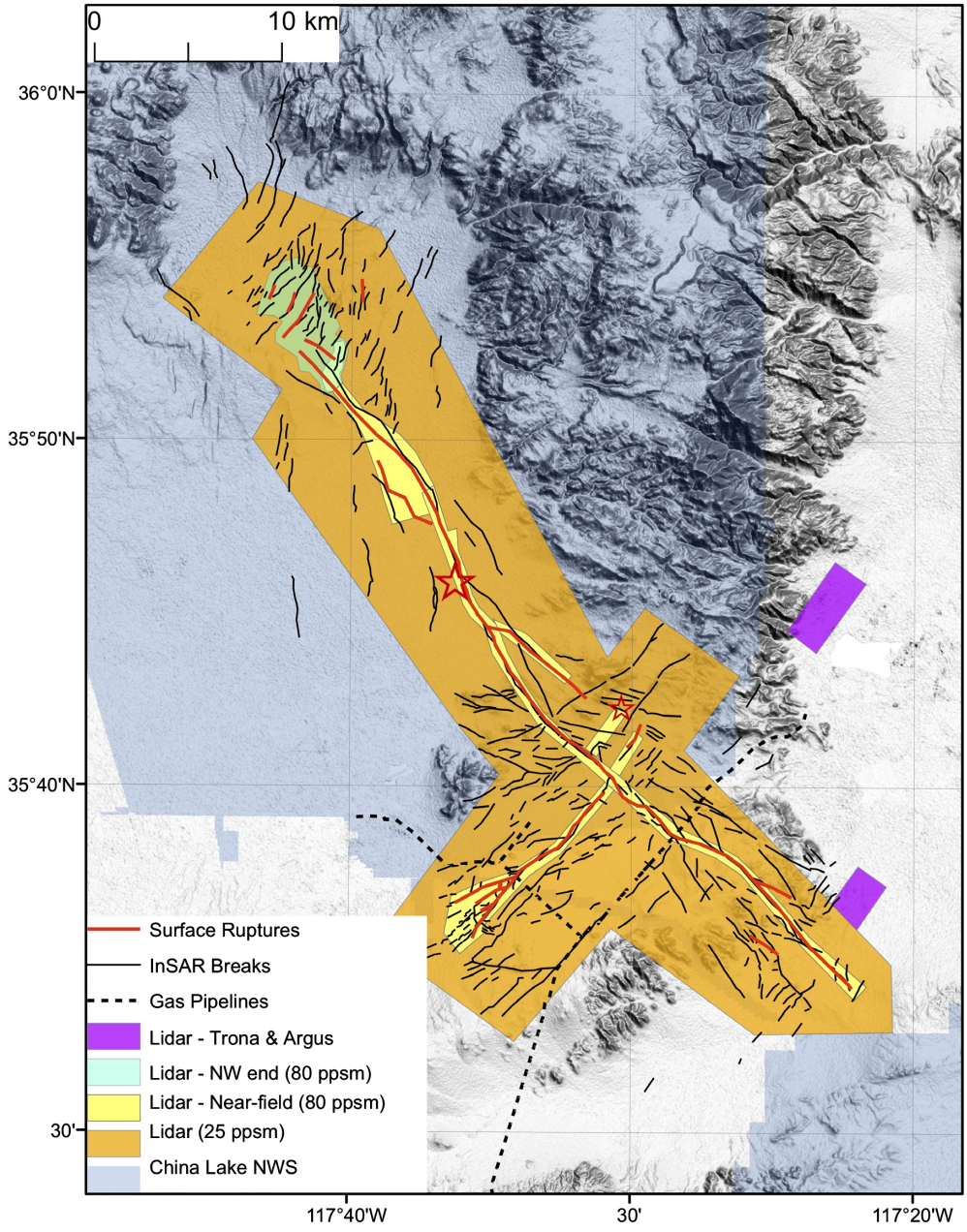

Figure 1. Areas-of-interest (AOI) polygons as defined by the committee that specified details of the acquisition plans. The colors indicate different portions of the light detection and ranging (lidar) acquisition plan as shown in the legend: (1) 25 ppsm is in both orange and magenta and (2) 80 ppsm is in both light yellow and light green. The red and dark gray lines show the fault surface rupture pattern known at the time of the survey planning (Kendrick *et al.*, 2019). The airborne geodata were entirely acquired by 2 August 2019 and subsequently, the surface rupture mapping has continued to clarify details of the fault rupture pattern (e.g., Ponti *et al.*, 2020). Base map is from Willis *et al.* (2019). InSAR, Interferometric Synthetic Aperture Radar; NWS, Naval Weapons Station. The color version of this figure is available only in the electronic edition.

have 4 ppsm (e.g., Arrowsmith and Zielke, 2009), which is insufficient for resolving geomorphic features offset by less than about half a meter. For the Ridgecrest earthquakes, the lidar acquisitions were generally more than five times more dense, and along the fault ruptures about 20 times more dense. Orthoimagery was also added for Ridgecrest, together greatly enhancing the resolving power for measuring offset features. Over the entire area encompassed by both the orange, light yellow, and light green polygons shown in Figure 1, overlapped-stereo aerial photographs were also acquired. These photos were orthorectified and projected onto the high-resolution topographic model derived from the lidar point cloud data, as specified in metadata. The ground sample distance of the orthoimagery product, as specified, is 5–10 cm.

A committee of U.S. Geological Survey (USGS) and National Science Foundation-funded (NSF) scientists drafted and then refined the AOI polygons shown in Figure 1, in accordance with field investigations and mapping based on satellite orthoimagery. Geological field work was conducted by a large team (e.g., Kendrick *et al.*, 2019; Ponti *et al.*, 2020), resulting in a synoptic overview of the main traces of surface fault ruptures. Early interpretations of satellite imagery, as well, helped to guide the field work, resulting in a timely, accurate representation of the fault surface rupture. This was used to specify AOI's for the high-resolution airborne geodata acquisition. The committee had to assess which were the primary and secondary fault ruptures, and on that basis had to perform cost-benefit trade-offs through discussion about optimization of the regions to be covered at different data resolutions with the airborne lidar and electro-optical orthoimagery.

The actual flight lines, "as flown," are shown in Figure 2. The realities of the acquisition necessarily took into account factors such as the topography and the boundaries of the

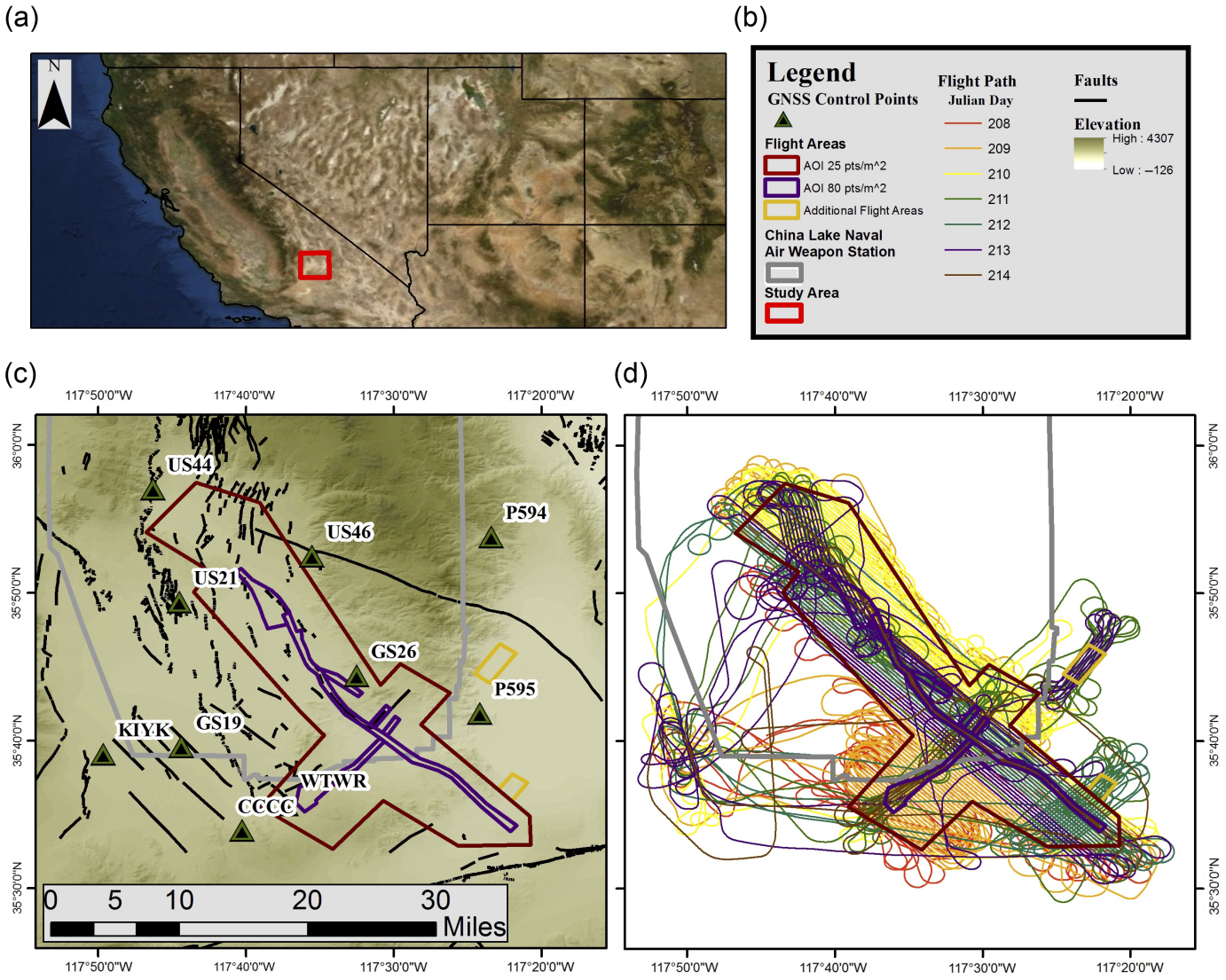

Figure 2. (a) Overview map with inset showing area of this study, (b) explanation to accompany next two portions of this figure, (c) primary Global Navigation Satellite Systems (GNSS) control points used for lidar survey, and (d) flight lines "as flown" by the National Center for Airborne Laser Mapping (NCALM) for this project. Relating to the AOI's in Figure 1, one can see that these flight lines optimized areal coverage and acknowledged the Navy range boundaries as a logistical constraint as well. Tight airspace coordination with the Navy, and a resultingly highly complex series of missions, involving multiple sorties per day, as early as dawn and as late as dusk, were required to accomplish this acquisition. The color version of this figure is available only in the electronic edition.

Navy base. During the data acquisition, it was necessary to coordinate with the Navy for operations in the China Lake restricted airspace to ensure that high-performance aircraft were not operating within the same airspace as the National Center for Airborne Laser Mapping (NCALM) aircraft, so as to avoid collision. This acquisition required special considerations to ensure pilot and aircraft safety, as well as all of the other usual factors such as air and ground crew logistical considerations, sensor and aircraft functionality, and weather. When loss of compression on one of our engines threatened to delay the entire project, timely assistance from personnel at Inyokern airport allowed us to locate the necessary parts, and one of our pilots made expedited repairs so that we could get back under way safely in hours rather than days.

Methods and Data

Methods for lidar and aerial digital camera data acquisition employed were guided by previous experience of the NCALM on other projects within the past several years (e.g., Fernandez-Diaz *et al.*, 2016), some of which had similar goals of quantifying fault zone geomorphology and earthquake rupture mapping. For this data set, details in this section override, yet are derived from, corrected from, and, in general, based closely upon web-based documentation from NCALM; see Data and Resources.

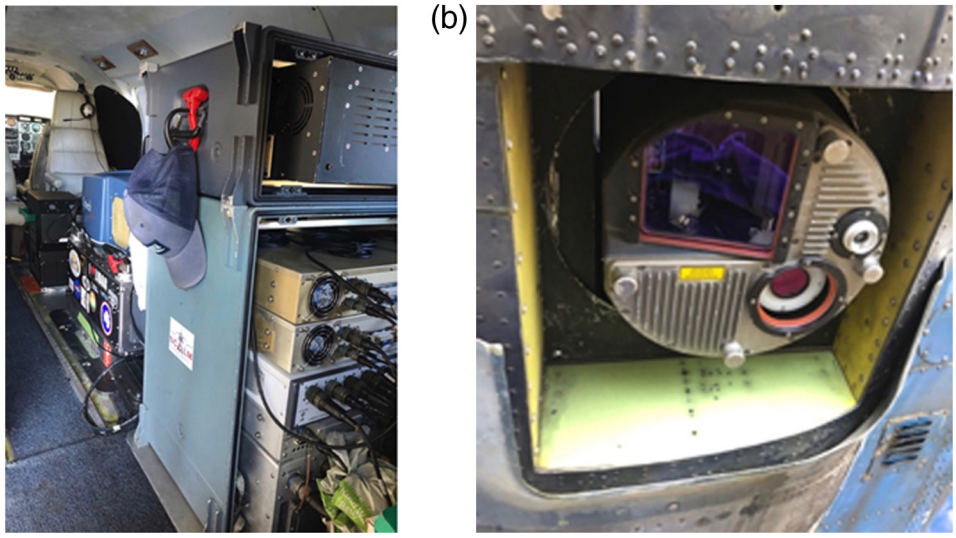

Figure 3. NCALM's airborne geodata sensor package, as installed on the aircraft. (a) The system includes all of the components listed and described in detail in Tables 2–4. The Optech Titan multispectral lidar system is contained within the blue unit that is mounted above the camera port, forward of the rack mount and aft of the seat. The rack-mount contains computers, data recorders, power supplies, and other vital system components. (b) Scanner and camera system sensor heads, as viewed through the opening of the camera port from beneath the belly of the aircraft. The color version of this figure is available only in the electronic edition.

In the upcoming four sections, we describe the instrumentation, processing, accuracy assessment, and data deliverables for this data acquisition. The NCALM airborne sensors and data acquisition system are described in the Data acquisition: instrumentation section. The Processing section describes the data processing system, beginning with processing of the GNSS and inertial measurement unit (IMU) data, and then the lidar, and finally the digital geodata processing. In the Lidar accuracy assessment section an accuracy assessment is provided; and in the Data deliverables section, specifics of the data deliverables, including metadata, are given in detail.

Data acquisition: instrumentation

Components, characteristics, settings, and nominal data parameters of the airborne sensor instrumentation package are given in the following photos (Fig. 3) and tables (see Fernandez-Diaz *et al.*, 2016 for further details). Table 1 gives data collection specifications for the Optech Titan multispectral lidar system, and Table 2 gives data

TABLE 1
Data Collection Specifications: Optech Titan Multispectral Lidar System (from Commissioning Report)

Parameter	Specification
Laser wavelength	Channel 1: 1550 nm, channel 2: 1064 nm, channel 3: 532 nm
Operating altitude*,†	300–2000 m AGL (1550 nm), 300–2500 m AGL (1064 nm), 300–2000 m AGL (532 nm)
Horizontal accuracy†	1/5500 × altitude(1σ)
Vertical accuracy†	<5–15 cm (1σ)
Minimum target separation	<1.0 m
Pulse repetition frequency	50–300 kHz (each wavelength)
Scan frequency	0–70 Hz
Scan angle	0–60° maximum
Beam divergence	0.5 mrad ($1/e^2$) (1550 nm), 0.5 mrad ($1/e^2$) (1064 nm), 1.0 mrad ($1/e^2$) (532 nm)
Range capture	Up to four range measurements for each pulse, including last
Intensity capture	12-bit dynamic measurement and data range
Image capture	Integrated digital camera

GNSS, Global Navigation Satellite Systems ; lidar, light detection and ranging.
*20% reflective target.
†Dependent on selected operational parameters using nominal 50° field of view in standard atmospheric conditions and good GNSS data quality

TABLE 2
Data Collection Specifications: DiMAC ULTRALiGHT + (i.e., Optech D-8900) Aerial Digital Camera (from DiMAC Datasheet)

Parameter	Specification
Sensor type	60 MP full-frame CCD, RGB
Sensor format (H × V)	8984 × 6732 pix
Pixel size	6 × 6 μm
Frame rate	1 frame/2 s
Lens focal length	70 mm
Filter	Color and near-infrared removable filters

CCD, charge-coupled device; DiMAC, digital modular aerial camera; RGB, red, green, blue.

TABLE 3
Technical Specifications: Optech Titan Multispectral Lidar System

Parameter	Specification
Position and orientation system	POS AV AP50 (OEM), 220-channel dual frequency
Laser classification	Class IV
Power requirements	28 V, 30 A, 800 W
Dimensions and weight	Sensor head: 630 × 540 × 450 mm, 65 kg; control rack: 650 × 590 × 490 mm, 46 kg
Data storage hard drives	Removable solid state disk SSD (SATA II)

OEM, original equipment manufacturer; POS AV, Positioning and Orientation System for Airborne Vehicles; SATA, Serial Advanced Technology Attachment; SSD, solid state drive.

collection specifications for the Digital Modular Aerial Camera (DiMAC) aerial digital camera system. Table 3 gives technical specifications for the Optech Titan multispectral lidar system, and Table 4 gives technical specifications for the DiMAC aerial digital camera system.

Processing

GNSS/IMU data processing. Reference coordinates (ITRF2014 Epoch 2019.500) for three primary stations, UNAVCO Plate Boundary Observatory Network of the Americas sites CCCC, P594, and P595 (locations shown in Fig. 2) were derived from observation sessions taken over the project duration and submitted to the National Geodetic Survey's online processor Online Positioning User Service, which processes static differential baselines tied to the international CORS network (see Data and Resources). The final solutions for these three GNSS control points were then used to compute reference coordinates for the seven temporarily occupied geodetic monuments, also shown in Figure 2 (GS19, GS26, KIYK, US21, US44, US46, and WTWR), from a network adjustment using multiple baseline occupations during the project duration in the GNSS network adjustment software package GrafNet (NovAtel, Inc.) (see Data and Resources).

TABLE 4
Technical Specifications: DiMAC ULTRALiGHT + Aerial Digital Camera

Parameter	Specification
FMC	Electromechanical, driven by Piezo technology
Shutter	Electromechanical iris mechanism, 1/125–1/500 s, *f*-stops: 4, 5.6, 8, 11, 16
Power requirements	24–28 V, 8 A, 168 W
Dimensions and weight	200 × 150 × 120 mm, ~4.5 kg
Data storage hard drives	500 GB removable solid state drives

Aircraft trajectories for all surveys were processed using the GrafNav software, which is a part of GrafNet (Novatel, Inc.). GrafNav uses GPS and Globalnaya Navigazionnaya Sputnikovaya Sistema dual-frequency phase history files of the reference and airborne receivers to determine a high accuracy, fixed integer, ionosphere-free differential solutions at a frequency of 1 Hz. All final aircraft trajectories are blended solutions from a minimum of four available reference stations dependent upon spatial coverage of the flight.

After GNSS processing, the 1 Hz trajectory solution and the 200 Hz raw IMU data, collected during the flights, are combined in APPLANIX software Position and Orientation System Package (POSPac) Mobile Mapping Suite (MMS). POSPac MMS implements a Kalman filter algorithm to produce a final, smoothed, and complete navigation solution including both aircraft position and orientation at 200 Hz. This final navigation solution is known as a smoothed best estimate of trajectory.

Lidar data processing. The following diagram (Fig. 4) shows a general overview of the NCALM lidar data processing workflow:

Classification. Classification is done by automated means, with manual validation, using Terrasolid software. NCALM makes every effort to produce the highest quality lidar data possible, but every lidar point cloud and derived digital elevation model (DEM) will have visible artifacts if it is examined at a sufficiently fine level. Examples of such artifacts (For a detailed discussion on the causes of data artifacts, and how to recognize them and a discussion of the procedures NCALM uses to ensure data quality; see Data and Resources.) include visible swath edges, corduroy (visible scan lines), and data gaps.

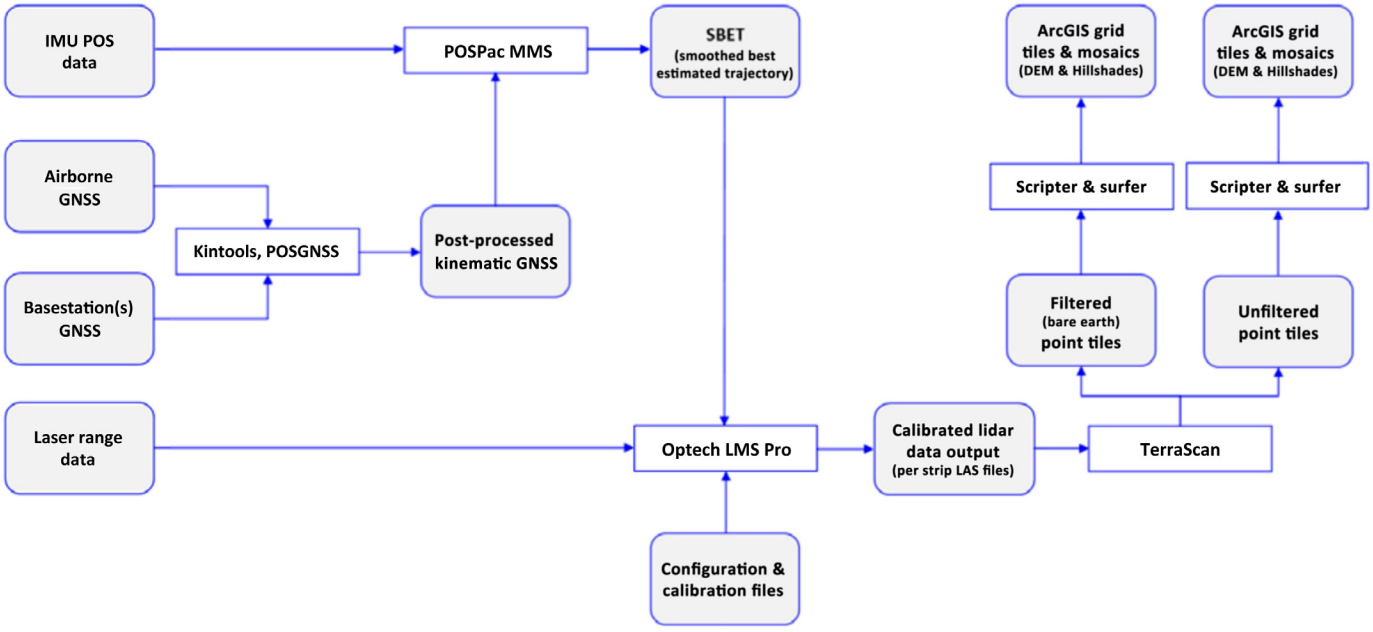

Figure 4. NCALM's typical lidar processing workflow. The color version of this figure is available only in the electronic edition.

Digital geodata processing. Digital geodata processing can be described in three steps: radiometric correction, calibration, and orthorectification. An overview of the processing steps is shown in the flowchart in Figure 5.

Calibration was performed on a set of images taken over a calibration site with perpendicular and opposing headings. Calibration involves using a bundle adjustment to solve for linear and angular misalignments with ground control points. For this purpose, the calibration site is located over an area with distinct road markings. The area surrounding Inyokern airport (KIYK) was used as the primary calibration site. Finally, the calculated misalignment values are fed back into the process to produce the orthorectified images.

DiMAC high-resolution visible geodata. Radiometric correction for DiMAC images involves fine tuning the white balance and exposure correction. This procedure is done using capture one image processing software (see Data and Resources). The next two steps of calibration through bundle adjustment and orthorectification are completed using TerraPhoto (currently version 19.006 [v.19.006]), part of the Terrasolid software suite.

Lidar accuracy assessment

System calibration of the sensor's three boresight angles (roll, pitch, and heading) and scanner mirror scale factor was performed by automated means using Optech LMS Pro software (currently v.4.4.0). Project lines and nonproject lines flown with opposite headings, combined with perpendicular cross lines, were used as input. These calibration values were then checked and recalculated on a flight-by-flight basis. After the calibration values were optimized, project flight lines were output and classified into ground and nonground classes. Surfaces were developed for each flight strip from the ground class points, and then these individual flight strip surfaces were differenced, and a value for the average magnitude of the height mismatch

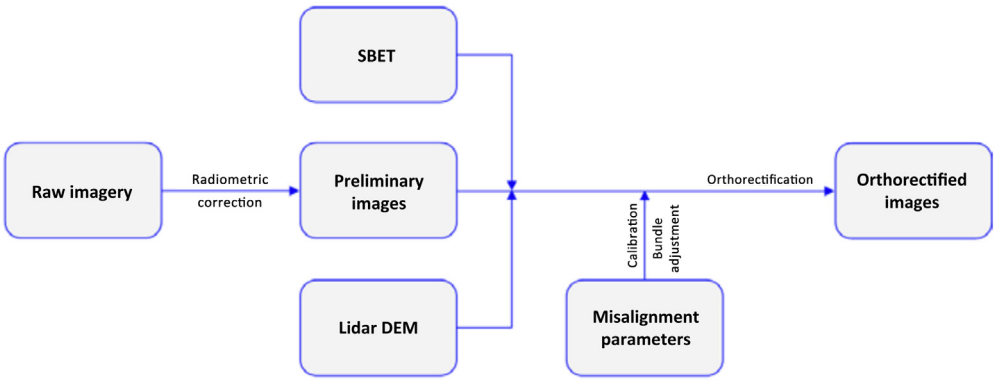

Figure 5. Geodata processing workflow. The color version of this figure is available only in the electronic edition.

(unsigned vertical differences between flight strips) over the entire project area was calculated.

Data deliverables

Here we describe details of the data files delivered by NCALM, and available from NCALM on their long-term archive (For users who access these data through OpenTopography, which serves the classified point cloud and rasters, this section describes files and file formats that are additionally available from NCALM.) including file formats and file naming conventions. We also provide additional related resources on LASer (LAS) files in particular for those needing to find further details about the LAS format.

Standard NCALM deliverables and file formats.

1. Point cloud in LAS format (v.1.4), classified with ground and nonground returns, in 1000×1000 m rectangular tiles.
2. ESRI FLT format 50 cm DEM from classified ground and bathymetry points.
3. ESRI-created Hillshade raster from the grid listed earlier.
4. ESRI FLT format 50 cm DEM from first-return points (canopy and buildings included).
5. ESRI-created Hillshade raster from the grid listed earlier.
6. Point cloud density image map.

File naming convention

LASer (LAS) files. The 1000×1000 m tiles follow a naming convention using the lower-left coordinate (minimum X, Y) as the seed for the file name as follows: XXXXXX_YYYYYYY. For example, if the tile bounds are the coordinate values from easting 550000 to 551000, and northing 4330000 to 4331000, and then the tile file name incorporates 550000_4330000 (see Data and Resources).

ESRI files. Because of the limited number of characters that can be used for ArcGIS data products, the resulting format is followed: XXX_YYYY_aabb. Again, the coordinates of the lower-left bound of the raster are used as the seed, for example, 4330_550. Here, the last digits are excluded to conserve characters. Next, the type of return used for creating the raster, represented as "aa," will be either "be" for bare earth (i.e., filtered or ground and bathymetry points) or "fr" for first return (i.e., unfiltered or default points). Finally, the raster-type of the file, represented by "bb," can be "gd" for a grid *.flt file or "hs" for a hillshade.

LAS file information. Each of the returns contained on the LAS tiles are encoded with a laser channel value. As previously noted, the Optech Titan has three channels: 1550, 1064, and 532 nm. The values used are 1 (1550 nm), 2 (1064 nm), and 3 (532 nm) and are stored in the user data record of the point data records in the LAS file. In addition, the classification values of the points follow the American Society for Photogrammetry and Remote Sensing standard (see Data and Resources). NCALM also includes the datum and projection information in the LAS file in the variable length records.

Metadata

Metadata for the surveys as well as quality metrics are available at the OpenTopography landing page for the dataset (see Data and Resources).

Data Dissemination

The lidar and aerial orthoimagery are freely available and distributed by OpenTopography (see Crosby *et al.*, 2019 for a recent overview). The primary data products from OpenTopography are the user-selected or bulk-downloaded point cloud files with DSM's or DEM's computed on the fly, 3D visualization in the browser, as well as precomputed DEM's and orthophoto rasters. These seamless data products are built on top of the NCALM deliverables described in the Standard NCALM deliverables and file formats section. Final products will be made available progressively using these same formats, conventions, and metadata.

Examples of the Data

In Figures 6–8 sample areas of the data set are demonstrated.

Discussion

The aerial geodata described in this article will be used as a basis for developing the final products of the fault rupture mapping effort. These efforts have been initially represented by Kendrick *et al.* (2019) and Ponti *et al.* (2020), using currently available base imagery. The expectation is that, for future-related efforts, the currently available fault rupture line work could later be adjusted so as to align with the geodata presented and described in this article. In addition, line work and feature digitization of the fault breaks that have already been done based on other imagery sources such as the reconnaissance mode photographs and a wide variety of satellite imagery could later be revised and redone using the lidar and orthoimagery products from this article. This could be done so as to fill in accurately the previous line work, and also to check in places with ground-based GPS and GNSS observations from the geologic team's field work, some of which have been obtained using base-station corrected GNSS so as to be accurate to the decimeter or even centimeter level. Such ground-based data may be used as a check for calibration and validation of the georeferencing of the geodata and image-derived products.

A space-based photogrammetric pre-event DEM is already available (Willis *et al.*, 2019) with which to compare these and other postevent geodata. We anticipate the geodata described in this article will help resolve the near- and far-field

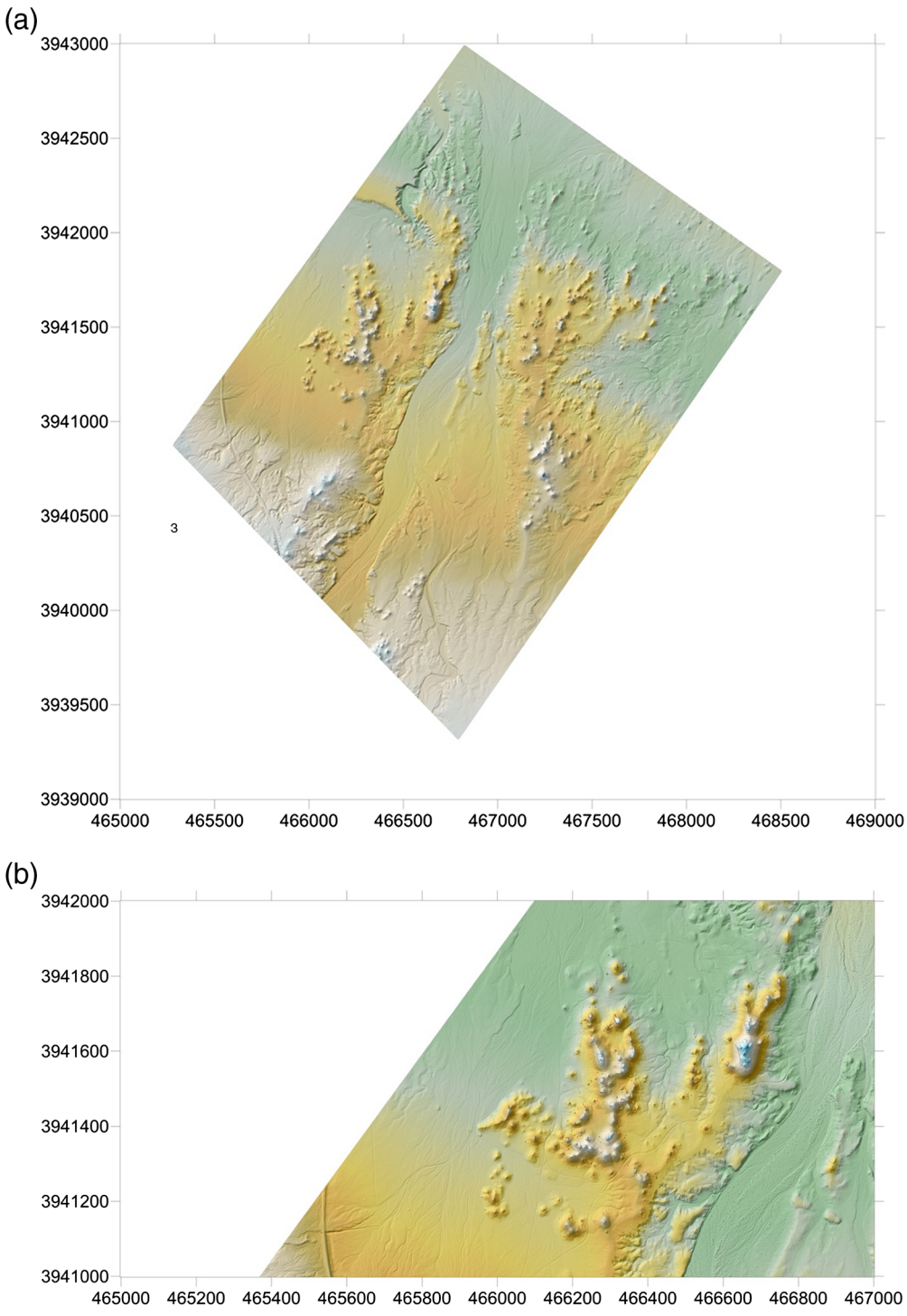

Figure 6. (a) Sample of the lidar data, showing the Trona Pinnacles area and surroundings. Zooming in portion of this area is shown next. (b) As described in Stewart *et al.* (2019, GEER-064), several of these fragile geological features sustained shaking-related damage as a result of the Ridgecrest earthquake sequence. These lidar data may augment unoccupied aircraft system-based structure-from-motion (SfM) products by, for example, providing a well-georeferenced and geodetic quality base image. Elevation scale is given in Figure 7. The color version of this figure is available only in the electronic edition.

deformation from the Ridgecrest earthquake sequence and form the basis of future investigations. This work could also form the basis of further airborne and satellite remote sensing investigations and help educate Department of Defense personnel on the impacts of earthquakes and surface fault ruptures on their facilities.

Conclusions

Geological surface rupture mapping rapidly defined the pattern of surface fault ruptures associated with the 2019 Ridgecrest earthquake sequence. One use of these data was to guide the aerial geodata collection described in this article. Three weeks after the mainshock, airborne geodata collection began, that is, we collected lidar topography and orthoimagery data as well as GPS ground control data. Over the course of seven days, often working from before sunrise until after sunset, two pilots took shifts and worked closely with the air and ground crews from NCALM and USGS. In all, we collected 650 km^2 of lidar at 25 ppsm, and 80 km^2 at 80 ppsm, plus orthoimagery at 5–10 cm ground sample distance over the area. Close coordination with the Navy ensured safe access to their restricted airspace for the duration of the data acquisition. The data are described here and samples are shown; the full geodata set will be made openly available through a combination of the OpenTopography website, which will have the lidar data and raster orthoimagery products, as well as the long-term NCALM archive for additional raw data files.

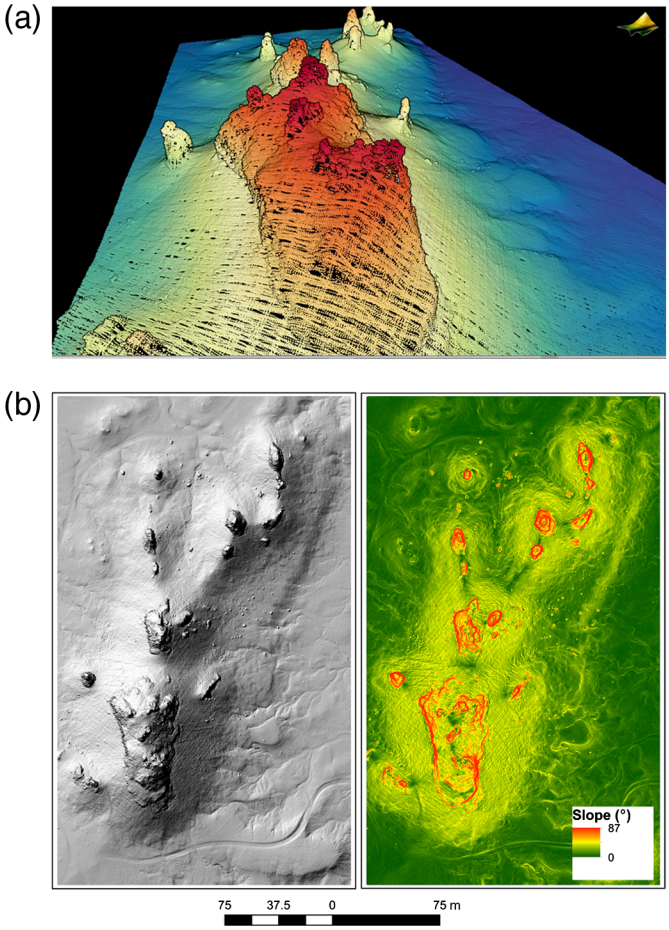

Figure 7. (a) Browser-based 3D point cloud visualization from OpenTopography site. Note the crossing laser scan lines. Perspective view over the Trona Pinnacles also shown in the next map, using a color gradient from 502 (blue) to 557 (red) m in elevation, and (b) 25 cm hillshade and slope map computed on demand in the OpenTopography site showing the Trona Pinnacles (see also 3D point cloud in prior figure). The color version of this figure is available only in the electronic edition.

Data and Resources

The data will all be made available at the following OpenTopography URL: Hudnut, K. W., B. Brooks, K. Scharer, J. L. Hernandez, T. E. Dawson, M. E. Oskin, R. Arrowsmith, C. A. Goulet, K. Blake, M. L. Boggs, S. Bork, C. L. Glennie, J. C. Fernandez-Diaz, A. Singhania, D. Hauser, S. Sorhus (2020). 2019 Ridgecrest, CA post-earthquake light detection and ranging (lidar) collection, National Center for Airborne Laser Mapping (NCALM), distributed by OpenTopography, available at doi: 10.5069/G97W69C0, 10.5069/G9W0942Z. Additional portions of the data set will be released pending additional review. Additional raw files may be accessed from the NCALM long-term archive, contact ncalm@egr.uh.edu; further information available at http://ncalm.cive.uh.edu/. Capture one image processing software is available at https://www.captureone.com/en/. The B4 lidar data are available in https://u.osu.edu/b4lidar/, https://doi.org/10.5066/F7TQ5ZQ6, and http://opentopo.sdsc.edu/lidarDataset?opentopoID=OTLAS.032018.32611.1. Documentation from NCALM is available at http://ncalm.cive.uh. For further information on Online Positioning User Service (OPUS), see https://www.ngs.noaa.gov/OPUS/ and for more information on the CORS network, see https://www.ngs.noaa.gov/CORS/. GrafNet Overview is available at https://docs.novatel.com/Waypoint/Content/GrafNet/GrafNet_Overview.htm. Current version of TerraScan v.19.019 is available at www.terrasolid.com/products/terrascanpage.php. A detailed discussion on the causes of data artifacts is available at ncalm.berkeley.edu/reports/GEM_Rep_2005_01_002.pdf and a discussion of NCALM procedures is available at ncalm.berkeley.edu/reports/NCALM_WhitePaper_v1.2.pdf. LASer (LAS) format description is available at https://www.loc.gov/preservation/digital/formats/fdd/fdd000418.shtml. American Society for Photogrammetry and Remote Sensing (ASPRS) and LAS formats are available at www.asprs.org/Committee-General/LASer-LAS-File-Format-Exchange-Activities.html. All websites were last accessed in March 2020.

Acknowledgments

The coauthors thank the U.S. Geological Survey and National Science Foundation (NSF) for providing the funding to National Center for Airborne Laser Mapping (NCALM) for this project and the authors especially also thank our pilots Robert Chalender and Greg McDonald and the aircraft vendor. Misty Ellingson and Andria Bullock, with support of Ole Hendon of Naval Air Warfare Center Weapons Division (NAWCWD) provided them with airspace access within the NAWSCL. The authors also benefitted greatly from the generosity of the Inyokern airport manager, Scott Seymour, and his staff who helped to locate parts and facilitate repair of the aircraft in their hangar. Mayor Peggy Breeden and Chief of Police Jed McLaughlin of the City of Ridgecrest opened their arms to our whole team while the authors worked in their city. Margo Allen, Helen Haase, Jeff Mayberry, Rob Gallagher, and Renee Hatcher, the team of Naval Air Weapons Station China Lake and NAWCWD Public Affairs Officers, tirelessly provided operational security review support to our whole team, as did the entire unexploded ordnance team. LT Angela Roush, U.S. Navy, and the R-2508 Joshua airspace controllers are also greatly thanked, as are California Highway Patrol and National Guard for helicopter support for the field work that allowed our flight line planning. The effective reconnaissance and geodata response resulted from several years of conference calls, e-mails, meetings, exercises, and planning. It took advanced planning, strategic thought, and coordination with other agencies. The important coordination role of the California Air Coordination Group, led by Derek Kantar of Caltrans, and of the California Earthquake Clearinghouse, co-led by Anne Rosinski and recently by Cindy Pridmore who co-led it, along with Heidi Tremayne, Maggie Ortiz-Millan, and others from Earthquake Engineering Research Institute, during the 2019 Ridgecrest sequence, and of its Overflight committee in particular, cannot be overstated. In addition, U.S. Department of the Interior's Office of Aircraft Services had established memoranda of understanding so that U.S. Geological Survey (USGS) personnel were able to safely conduct multiple aerial reconnaissance and geodata missions. Thanks to the NCALM processing team and the OpenTopography team for making these data available rapidly. Many thanks to the Southern California Earthquake Center (SCEC) headquarters who helped support the Rapid Response

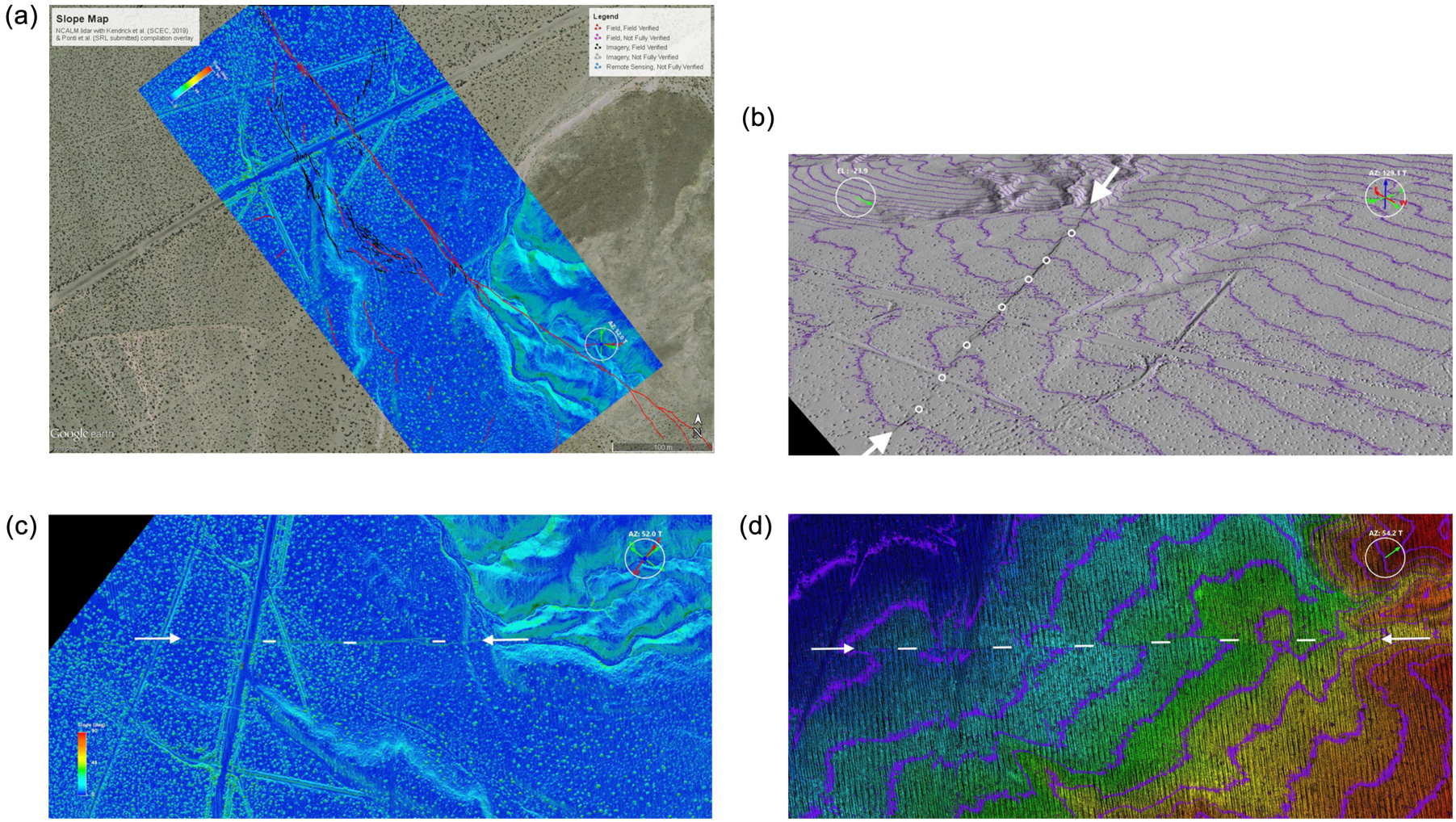

Figure 8. Lidar data showing scarp and offset geomorphology along the mainshock surface fault rupture, centered at a location 0.4 km to the southeast of where the rupture crosses Highway 178 (Trona Road). (a) Inset showing slope map and surface fault ruptures as mapped by Kendrick *et al.* (2019) and Ponti *et al.* (2020), which included imagery and data from Pierce *et al.* (2019) and Stewart *et al.* (2019). (b) View toward the southeast across the scarp, showing a hillshade of the topography along the fault scarps as well as 1.0 m contour lines (in purple), (c) nadir view of the slope map show in (a), but rotated, zoomed in, and without the mapped fault traces so as not to bias interpretation of features, and (d) same nadir viewpoint as in (c), but showing the raw lidar point cloud and 1.0 m contour lines. Note that offsets of some geomorphic features, such as the primary fault scarp, appear well resolved by the contour line breaks. White dashed lines indicate approximate trace of main fault rupture trace. The features such as road berms and traces of underground infrastructure made by humans tend to be sharper and even better resolved than the natural, more rounded features. The color version of this figure is available only in the electronic edition.

Research (RAPID) award from the U.S. NSF. OpenTopography is supported by the U.S. NSF under Award Numbers 1833703, 1833643, and 1833632. Important Global Navigation Satellite Systems (GNSS) data from stations CCCC, P594, and P595 were provided by the Geodetic Facility for the Advancement of GEoscience (GAGE), operated by UNAVCO, Inc., with support from the NSF and the National Aeronautics and Space Administration under NSF Cooperative Agreement EAR-1724794. The authors also thank the reviewers of this article, Andrew Meigs, James Hollingsworth, Beth Haddon, and Dan Opstal for improving the article.

Any use of trade, product, or firm names is for descriptive purposes only and does not imply endorsement by the U.S. Government.

References

Arrowsmith, J. R., and O. Zielke (2009). Tectonic geomorphology of the San Andreas Fault zone from high resolution topography: An example from the Cholame segment, *Geomorphology* **113,** doi: 10.1016/j.geomorph.2009.01.002.

Baize, S., F. Nurminen, A. Sarmiento, T. Dawson, M. Takao, O. Scotti, T. Azuma, P. Boncio, J. Champenois, F. R. Cinti, *et al.* (2019). A worldwide and Unified Database of Surface Ruptures (SURE) for fault displacement hazard analyses, *Seismol. Res. Lett* **91,** no. 1, 499–520.

Bevis, M., K. Hudnut, R. Sanchez, C. Toth, D. Grejner-Brzezinska, E. Kendrick, D. Caccamise, D. Raleigh, H. Zhou, S. Shan, *et al.* (2005). The B4 project: Scanning the San Andreas and San Jacinto fault zones, *AGU FM05*, San Francisco, California, December 2005, H34B–01.

Borsa, A., and J.-B. Minster (2012). Rapid determination of near-fault earthquake deformation using differential LiDAR, *Bull. Seismol. Soc. Am.* **102,** no. 4, 1335–1347, doi: 10.1785/0120110159.

Crosby, C. J., J. R. Arrowsmith, and V. Nandigam (2019). Zero to a trillion: Advancing surface process studies with open access to high resolution topography, in *The Remote Sensing of Geomorphology*, Developments in Earth Surface Processes, P. Tarolli and S. Mudd (Editors), Elsevier, Amsterdam, The Netherlands, ISBN-13: 9780444641779.

Duffy, B., M. Quigley, D. J. A. Barrell, R. Van Dissen, T. Stahl, S. Leprince, C. McInnes, and E. Bilderback (2013). Fault kinematics and surface deformation across a releasing bend during the 2010 MW 7.1 Darfield, New Zealand, earthquake revealed by differential LiDAR and cadastral surveying, *GSA Bull.* **125,** nos. 3/4, 420–431, doi: 10.1130/B30753.1.

Fernandez-Diaz, J. C., W. E. Carter, C. Glennie, R. L. Shrestha, Z. Pan, N. Ekhtari, A. Singhania, D. Hauser, and M. Sartori (2016). Capability assessment and performance metrics for the titan multispectral mapping lidar, *Rem. Sens.* **8,** 936, available at https://www.mdpi.com/2072-4292/8/11/936 (last accessed March 2020).

Glennie, C. L., A. Hinojosa-Corona, E. Nissen, A. Kusari, M. E. Oskin, J. R. Arrowsmith, and A. Borsa (2014). Optimization of legacy lidar data sets for measuring near-field earthquake displacements, *Geophys. Res. Lett.* **41,** doi: 10.1002/2014GL059919.

Hudnut, K. W., A. Borsa, C. Glennie, and J.-B. Minster (2002). High-resolution topography along surface rupture of the 16 October 1999 Hector Mine, California, earthquake (Mw7.1) from airborne laser swath mapping, *Bull. Seismol. Soc. Am.* **92,** no. 4, 1570–1576.

Kendrick, K., A. Sinan, A. Steve, A. Jean-Philipe, B. Scott, B. Kelly, B. Stephan, B. Ben, B. Paul, C. Colin, *et al.* (2019). Preliminary geologic observations of the Ridgecrest M6.4 and M7.1 earthquake sequence, *Annual Meeting of the Southern California Earthquake Center*, Palm Springs, California, September 2019, Abstract #217.

Nissen, E., A. K. Krishnan, J. R. Arrowsmith, and S. Saripalli (2012). Three-dimensional surface displacements and rotations from differencing pre- and post-earthquake LiDAR point clouds, *Geophys. Res. Lett.* **39,** L16301, doi: 10.1029/2012GL052460.

Oskin, M. E., J. R. Arrowsmith, A. Hinojosa Corona, A. J. Elliott, J. M. Fletcher, E. Fielding, P. O. Gold, J. J. Gonzalez Garcia, K. W. Hudnut, O. Kreylos, *et al.* (2012). Near-field deformation from the El Mayor-Cucapah earthquake revealed by differential LiDAR, *Science* **335,** no. 6069, 702–705, doi: 10.1126/science.1213778.

Pierce, I., A. Williams, R. D. Koehler, and C. Chupik (2019). High resolution structure-from-motion models and orthophotos of the southern sections of the 2019 Mw7.1 and Mw6.4 Ridgecrest earthquakes surface ruptures, *Seismol. Res. Lett* doi:10.1785/0220190289.

Ponti, D. J., J. Luke Blair, C. M. Rosa, K. Thomas, A. J. Pickering, S. Akciz, S. Angster, J.-P. Avouac, J. Bachhuber, S. Bacon, *et al.* (2020). Documentation of surface fault rupture and ground deformation features produced by the Ridgecrest M6.4 and M7.1 earthquake sequence of July 4 and 5, 2019, *Seismol. Res. Lett.*

Quigley, M., R. Van Dissen, N. Litchfield, P. Villamor, B. Duffy, D. Barrell, K. Furlong, T. Stahl, E. Bilderback, and D. Noble (2012). Surface rupture during the 2010 Mw 7.1 Darfield (Canterbury) earthquake: Implications for fault rupture dynamics and seismic-hazard analysis, *Geology* **40,** no. 1, 55–58, doi: 10.1130/G32528.1.

Scott, C., J. Champenois, Y. Klinger, E. Nissen, T. Maruyama, T. Chiba, and R. Arrowsmith (2019). The 2016 M7 Kumamoto, Japan, earthquake slip field derived from a joint inversion of differential lidar topography, optical correlation, and InSAR surface displacements, *Geophys. Res. Lett.* **46,** 6341–6351, doi: 10.1029/2019GL082202.

Scott, C. P., J. R. Arrowsmith, E. Nissen, L. Lajoie, T. Maruyama, and T. Chiba (2018). The M7 2016 Kumamoto, Japan, earthquake: 3-D deformation along the fault and within the damage zone constrained from differential lidar topography, *J. Geophys. Res.* **123,** 6138–6155.

Stewart, J. P., S. J. Brandenberg, P. Wang, C. N. Chukwuebuka, K. Hudson, S. Mazzoni, Y. Bozorgnia, K. W. Hudnut, C. A. Davis, *et al.* (2019). Preliminary report on engineering and geological effects of the July 2019 Ridgecrest Earthquake sequence, *Geotechnical Extreme Event Reconnaissance Association Rept. GEER-064 (v.2)*, doi: 10.18118/G6H66K.

Willis, M. J., W. D. Barnhart, R. Cassotto, J. Klassen, J. Corcoran, T. Host, B. Huberty, K. Pelletier, and J. F. Knight (2019). CaliDEM: Ridgecrest, CA region 2m digital surface elevation model, *Funding by NSF and USGS, Data collection by DigitalGlobe*, Distributed by OpenTopography, doi: 10.5069/G998854C.

Manuscript received 28 October 2019
Published online 22 April 2020